Tailoring the squalene-hopene cyclase for stereoconvergent and efficient cationic cyclization cascades

Andreas Schneider[1†], Christian Curado[2†], Thomas B. Lystbaek[1], Sílvia Osuna[2,3*] & Bernhard Hauer[1*]

[1]Department of Technical Biochemistry, Institute of Biochemistry and Technical Biochemistry, University of Stuttgart, Stuttgart-Vaihingen, Germany

[2]CompBioLab Group, Institut de Química Computacional i Catàlisi and Departament de Química, Universitat de Girona, Girona, Spain

[3]ICREA, Barcelona, Spain

*Correspondence to: silvia.osuna@udg.edu and Bernhard.Hauer@itb.uni-stuttgart.de

[†]the authors contributed equally

Abstract

Asymmetric catalysis has witnessed paramount lessons from terpene cyclase enzymology such as the ability to control dynamic carbocations or cationic cyclization cascades. In general, these cascades are stereodivergent and thus rely on the terpene's double-bond geometry. In this work, we illuminate how the dynamic supramolecular framework of squalene-hopene cyclases (SHCs) can be tailored to break with this paradigm. Creating a locally electron-enriched confined active site, we enabled the stereoconvergent cationic cyclization of a *cis*/*trans* terpene mixture into one isomer. Our results suggest that a priorly unknown active site "memory" effect of the SHC aids this intricate transformation. Based on these findings, we employed synergistic active site and tunnel engineering to generate a most efficient (–)-ambroxide cyclase. Broad computational investigations evidently explain how the introduced mutations work in concert to improve substrate acquisition, flow and chaperoning. Nonetheless, kinetics disclosed a substrate-induced downregulation of the membrane-bound SHC as the major turnover limitation *in vivo*. Merging these new insights with the improved and stereoconvergent catalysis of the enzyme, we applied a feeding strategy to exceed 10^6 TTN with the SHC.

Introduction

The disclosure of the first terpene cyclase crystal structures in 1997 represents a landmark in cyclase history, allowing scientists deep structural insights and functional investigations on how nature creates molecular diversity in terpenes.[1–3] Since then, computational models constantly elucidate the enzymes' unique conformational control over dynamic carbocations in concerted rearrangement cascades exhibited by their highly confined polyfunctional active sites.[4–6] Mutagenesis studies within these active sites revealed how to manipulate cationic cyclization cascades in a target-oriented manner[7,8] and presented precisely positioned water molecules as pivotal for catalysis.[9,10] Furthermore, extensive substrate scope surveys showcased the ability of certain cyclases, such as the squalene-hopene cyclase (SHC), to accept dozens of terpenes[11–16] and catalyze non-natural transformations, e.g. a Friedel-Crafts alkylation or a Prins reaction.[17–19] Despite this tremendous progress, one persistent limitation employing cyclases, is the strict double-bond isomerism of the linear precursor that governs the fate of the successive sp^3 stereocenter in the cyclic product (**Figure 1A**).[8,20,21] As a result, the application requires preceding separation of the *E*/*Z* isomeric substrate mixtures, which is tedious and costly.[22,23] Therefore, a cationic cyclization exhibiting stereoconvergence is on top of chemists wish lists.

Considering the supramolecular level, few is known about the dynamic behavior of triterpene cyclases, such as SHCs, during catalysis as both the apo and substrate-bound conformation are identical.[1,24] Other than that, an induced-fit mechanism was suggested in class I terpene cyclases.[25] Furthermore, SHCs comprise a unique role in enzymology as monotopic membrane-bound enzymes, accounting for only 0.06% of all crystallized protein structures (**Figure 1B**).[26] Nature evolved these interfacial allocated enzymes to provide them the catalytic skills of their soluble congeners but with the additional ability to source highly hydrophobic C30 squalene from their host's biomembrane. In fact, SHCs regulate their biological host's membrane integrity by depositing generated pentacyclic hopenes in the membrane interior.[27–29] Vice versa, seminal theoretical as well as practical studies indicate

that the activity of membrane-bound enzymes relies on the current state of the membrane integrity, which is drastically influenced by terpenes.[30–35] This aspect may contribute to the second persistent limitation of cyclases, which is their generally low catalytic performance (TTNs below 10^3 [8,21,36]) compared to other enzyme families, such as monooxygenases, transaminases or lipases with TTNs in the range of $10^{5\text{-}7}$.[37]

In this work, we addressed both limitations currently given in SHC catalysis. Inspired by the recent success in conformational control over reactive intermediates,[38,39] we envisioned that the strong confinement of SHCs active site could be leveraged to perform an unprecedented stereoconvergent cationic cyclization of a *cis*/*trans* isomeric substrate mixture. Such a mechanism should be generally feasible considering the work of Tiefenbacher et al. that suggested a direct *transoid-cisoid* rotation during the cationic rearrangement of geranyl acetate inside a supramolecular host.[40,41] Moreover, acknowledging the membrane-bound nature of SHCs, we aimed to investigate the potential downregulation by kinetically contrasting the SHC in artificial membrane-bound (*in vitro*) and biomembrane-bound (*in vivo*) state.

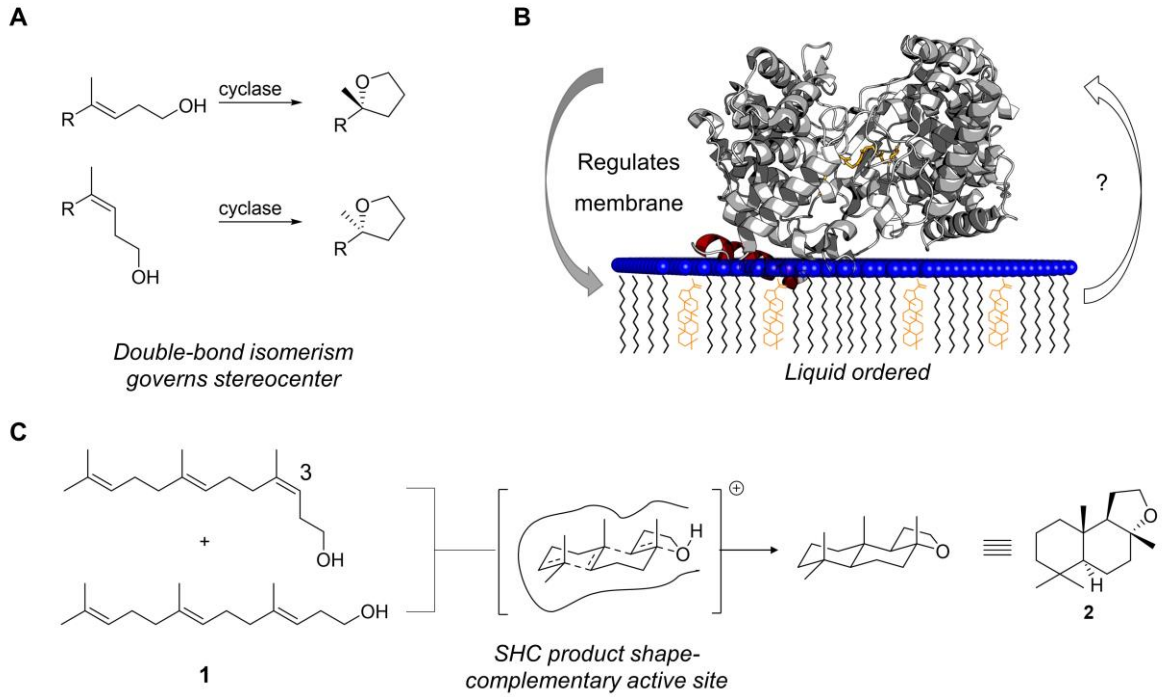

Figure 1: Current issues in SHC catalysis. (**A**) The stereoselectivity of terpene cyclases is generally governed by the *E* or *Z* double-bond isomerism of their substrates.[20,21] (**B**) SHCs (grey cartoon) are bound to their host's biomembrane (blue headgroups and by a reentrant α-helix (red cartoon), which classifies them as monotopic

membrane enzymes.[26] Naturally, they regulate the biomembrane's integrity by producing hopenes (yellow scaffolds) to counteract exterior stresses, e.g., temperature fluctuations or molecular toxifications by lipophilic molecules.[29] In turn, a membrane-bound enzymes activity is dependent on the structural integrity of the biomembrane.[32–35] (**C**) The herein chosen model reaction of an isomeric 3*E*/3*Z*-mixture of homofarnesol **1** to (–)-ambroxide **2** via a stereoconvergent cationic cyclization.

As a model reaction for this endeavor, we chose the archetypical promiscuous cyclization of homofarnesol **1** to (–)-ambroxide **2** (**Figure 1C**). This reaction offers several advantages and opportunities: (a) Catalysis has been shown to work both *in vitro* and *in vivo*.[11,36,42,43] (b) As product **2** solely crystallizes from the reaction broth, absolute selectivity towards **2** can be leveraged to overcome potential terpene-induced downregulation. (c) Product **2** is one of the highest valued fragrances in the industry and the *Aac*SHC (short: *Aac*) catalyzed highly stereoselective cyclization of homofarnesol **1** towards **2** provides a potent substitute for the scarce natural resource of **2**.[44] Especially, given the fact that chemical catalysts need harsh conditions and are far inferior in terms of selectivity (50% *ee* and 64% *de*).[45] These facts render the promiscuous cyclization of **1** ideally suited for a comprehensive investigation on SHC catalysis to cross its current catalytic boundaries.

Results and discussion

Mechanistic elucidation of a stereoconvergent cationic cyclization aided by active site "memory" of the squalene-hopene cyclase.

The requirements for a stereoconvergent cyclization of isomerically mixed **1** encompass a product **2** shape-like confined active site and the lifetime for a carbocation to undergo *cisoid-transoid* bond rotation.[46] The natural tricyclic shape-complementarity for **2** of the *Aac*'s active site was already demonstrated[42,47] and grants highly selective cyclization of *E*,*E*-**1** towards major product **2** and minor diastereomer **3**, whereas *Z*,*E*-**1** isomer was shown to result in side products **4** and **5** (**Figure 2A**).[36] We speculated that if we tune the electron density in close proximity to the C3-C4 double-bond, where the transient carbocation needs to flip, we could extend its lifetime to perform the desired *cisoid-transoid* bond rotation during the tricyclization.[48,49] To that end, we docked *E*,*E*-**1** into the active site of the crystal structure of

the *Aac* and chose three amino acid positions W169,G600 and F601 for site-saturation mutagenesis (**Figure 2B,** orange sticks). Furthermore, we exploited the natural diversity of SHCs with four homologs *Zmo*1, *Zmo*2, *Sco* and *Tel*, exhibiting subtle changes around the desired double-bond (**Figure 2B,** green sticks, Figure S1). Besides the *Z*,*E* isomeric mixture (55% *E*,*E*-**1**, i.e., mix-**1**), we tested the *E*,*E* enriched (95% *E*,*E*-**1**, i.e., *E*,*E*-**1**) substrate mixture to identify enzymes that improve the *E*,*E* pre-folding which results in the desired product (**Figure 1C**, transition state).

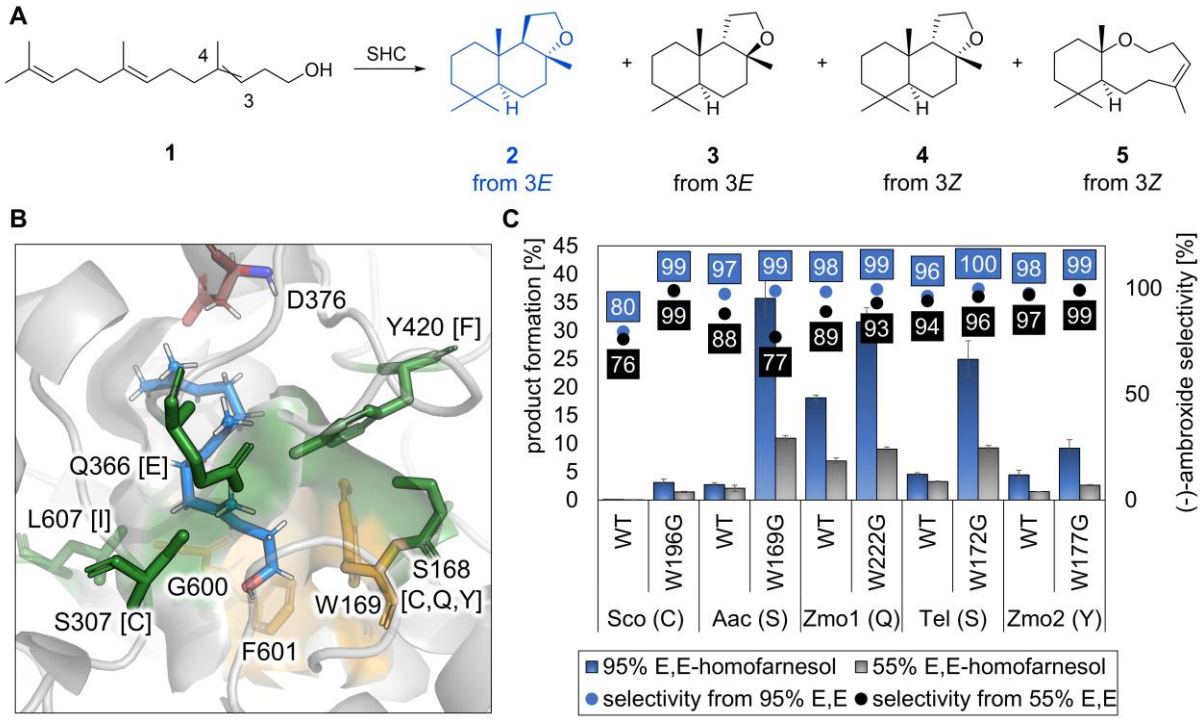

Figure 2: Elucidation of a stereoconvergent cationic cyclization enabled by the SHC. (**A**) The SHC-mediated cyclization of *E*,*E*-**1** results in desired product **2** (blue scaffold) and **3**, whereas cyclization of Z,E-1 results in products **4** and **5**. (**B**) *E,E*-**1** (blue sticks) docked into the active site of the *Aac* (PDB: 1UMP). Catalytic aspartate shown as red sticks. Amino acids shown as green sticks represent the natural diversity given as one-letter code in brackets at the distinct position. Amino acids shown as orange sticks were chosen for site-randomization. (**C**) SHC catalyzed stereoselective and stereoconvergent cyclizations of *E*,*E*-**1** enriched (blue bars and spots) and **1** isomeric mix (black bars and spots). (–)-ambroxide **2** selectivity was calculated by dividing formed **2** by all side products. Amino acid at position 168 (*Aac* counting) is given in brackets after the respective homolog. Reaction conditions: 10 mM **1**, *E. coli* cells expressing SHC with OD_{600} = 10 (~20 mg_{CDW}/mL), *dd*H_2O 1% DMSO, 30 °C, 20 h. Error bars represent the s. d. of technical triplicates. Similar expression was determined via SDS-PAGE. *Zmo*2 showed lower expression compared to other SHCs. The use of isolated enzymes did not produce acceptable results, as *Zmo*1, *Zmo*2 and SHCs were inactive in the chosen CHAPS membrane-mimic environment.

Starting with the homologs and using *E*,*E*-**1**, most SHC WTs exhibited excellent **2** selectivities of >95% as expected with modest product formations of 3-18% during the *in vivo*

biotransformation in the order *Aac*<*Zmo*2<*Tel*<*Zmo*1 (**Figure 2C**, WTs, blue bars and spots). The homolog from *Sco* showed only 0.1% product formation and comparatively poor selectivity of 80%. The unique difference of this congener is the hydrophobic cysteine at position 168 (*Aac* counting, Figure S1). Encouraged by these results, we tested mix-**1** and to our delight, all SHC WTs naturally exhibited stereoconvergence of 76-97% towards product **2** in the order *Sco*<*Aac*<*Zmo*1<*Tel*<*Zmo*2 with product formations of 0.1-7% in the order *Sco*<*Aac*<*Zmo*2<*Tel*<*Zmo*1 (**Figure 2C**, black bars and spots). Closer inspection of the position 168, suggested that the ability of stereoconvergence increased with the electron density at this position that is effectively accessible for the C3-C4 double bond: *Sco* (cys)<*Aac* (ser)<*Zmo*1 (gln)<*Tel* (ser)<*Zmo*2 (tyr). Please note that the *Aac* is the only homolog with a tyr at position 420, which may sterically hinder the access to position 168 (Figure S2). Site-saturation of the *Aac* resulted in variant W169G with 13-fold increased product formation and 99% **2** selectivity using *E*,*E*-**1** (for more hits see Figure S3). Employing mix-**1**, product formation also increased 5-fold, however, stereoconvergence decreased from 88% to 77%. The beneficial W169G mutation was subsequently transferred to the SHC homologs, thus allowing large jumps in sequence space of the SHC active site. Gratifyingly, the mutation of the conserved tryptophane (Figure S4) to glycine increased product formation by up to 13-fold (*Sco*<*Zmo*2<*Tel*<*Zmo*1<*Aac*) and stereoselectivity for **2** using *E*,*E*-**1** to >99% for all SHCs (**Figure 2C**, 'W to G' variants, blue bars and spots). Employing mix-**1**, product formation also increased by up to 5-fold (*Sco*<*Zmo*2<*Tel*~*Zmo*1<*Aac*) and stereoconvergence for **2** increased by up to 99% for congeners *Sco* and *Zmo*2 (**Figure 2C**, 'W to G' variants, black bars and spots). Noteworthy, we identified the generated 'hole' by the 'W to G' mutation as a potential water trapping site, which may provide its electron density to the carbocation and may support in pre-folding of **1** (Figure S5). Next, we performed a comprehensive mutation exchange within the homologs *Aac*, *Tel* and *Zmo*1, which emphasized the important phe at position 420 (*Aac* counting) and enriched electron density around the C3-C4 double-bond combined with strong confinement as subtle changes in one of these properties lowered the stereoconvergence down to 68% (Figure S6). These results further disclosed *Tel*W172G as the most active and

selective catalyst and thus we selected this enzyme for a detailed inspection of the reaction conditions on the stereoconvergence.

Following the mix-**1** reaction over time at 30 and 40 °C, revealed a faster cyclization at higher temperature, almost even depletion of both isomers over time and no temperature influence on the convergence (Figure S7). Moreover, we performed the biotransformation of mix-**1** with isolated *Te*W172G and in deuterium-labeled water, which suggested that this delicate mechanism proceeds via a single protonation and is performed in the enzyme's active site rather than by *E. coli* (Figure S8). However, when we successively varied the 3*E*:3*Z*-ratio of **1** in favor of the *Z*-isomer, the enzyme surprisingly lost its unique convergence and activity (**Table 1**), which is why we invoked the mnemonic enzyme model in explaining.[50]

Table 1: *E/Z*-ratio dependent stereoconvergent cyclization of **1**. Reaction conditions: 10 mg_{CDW}/mL *E. coli* cells expressing SHC, 10 mM substrate **1**, *dd*H_2O, 1% DMSO, 30 °C, 600 rpm.

E,E-**1** [%]	*Z,E*-**1** [%]	**2** [%]	side products [%]	product formation [%]	time [h]
90	10	99.9	0.1	60	20
60	40	99.7	0.3	58	20
55	45	99.5	0.5	48	20
34	66	97	3	42	20
25	75	93	7	45	24
1	99	34	66	5	20

This model exists since the 1960s[51] and states that a substrate turnover is not independent from the earlier one as it induces a conformational change of the enzyme to a more rigid lock-and-key conformation,[52–54] which confers it the ability of an active site "memory". Based on this model, we varied the ratio of mix-**1** to *Te*W172G concentration what unambiguously resulted in a drop of the convergence to 87% using high catalyst loading (**Table 2**).

Table 2: Catalyst/substrate-concentration ratio dependent stereoconvergent cyclization of **1**. Reaction conditions: 55:45 *E/Z*-substrate **1**, *dd*H_2O, 1% DMSO, 30 °C, 48 h, 600 rpm.

cells [mg_{CDW}/ml]	mix-**1** [mM]	**2** [%]	side products [%]	product formation [%]
50	50	99	1	24
50	10	87	13	85
10	10	99.9	0.1	45
10	2	86.9	13.1	86

With this knowledge in hands, we screened our SHC library for similar mnemonic enzyme aided stereoconvergence of *E*/*Z*-geranyl acetone **3** and found *Aac* variant L607F. This enzyme is highly selective for the bicyclization of *E*-**3** towards *E*-**4** and poorly active using Z-**3**. Leveraging the elucidated effect, the enzyme cyclized 81% of a 60:40 *E*/*Z*-**3** mixture towards >98% *E*-**4**, which further strengthened our hypothesis (**Scheme 1**).

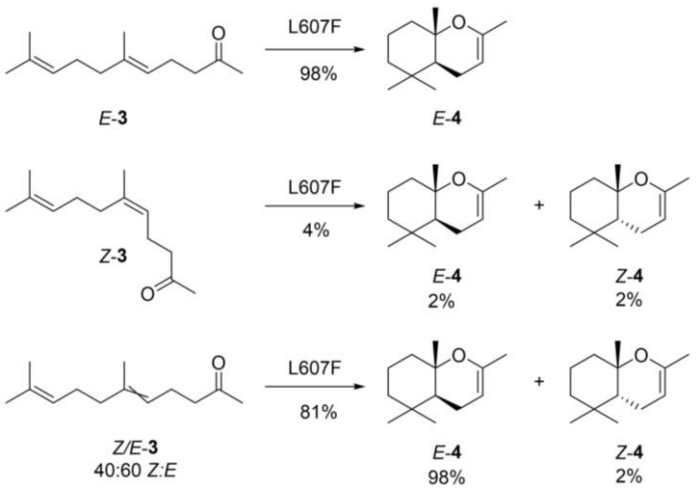

Scheme 1: Stereoconvergent cyclization of *E*/*Z*-**3** using *Aac* L607F. Reaction conditions: 10 mg_{CDW}/mL *E. coli* cells expressing SHC, 2 mM substrate **3**, *dd*H_2O, 1% DMSO, 30 °C, 60 h, 600 rpm. Product formations were determined via standard curves. See supporting chromatograms for more detail.

In summary, our results evidently led us to the proposed mechanism in **Figure 3**: After the biomolecular recognition of *E*,*E*-**1** the dynamic SHC enters the energetically most favorable product-**2**-shape-like stiff conformation. In this conformation, the enzyme achieves isomerization of the "wrong" substrate *Z,E*-**1** by balancing confinement and local electron density around the transient carbocation. As long it can sustain this conformation by incoming *E*,*E*-**1**, the cyclization of mix-**1** will be stereoconvergent as all "wrong" substrates are masked by *E*,*E*-**1** (Figure S9). The *E*:*Z* and enzyme:substrate ratio experiments strengthen this hypothesis. After full conversion, the enzyme relaxes back to the native dynamic conformation. Remarkably, all SHCs exhibited the ability of convergently cyclizing mix-**1**, which presumably derives from the natural squalene cyclization mechanism. This mechanism includes an unusual 1,2-alkyl shift of the C-ring, forming an unstable secondary carbocation, which requires electron density to survive that may be provided by the S168-site (Figure S10). We assume

that, a potentially trapped water molecule is now part of the cyclization mechanism, which is underpinned by an identified water channel behind position 168[55] and reminiscent of the cationic rearrangement mechanism of the bornyl diphosphate synthase that also includes a trapped water molecule and a *transoid-cisoid* bond rotation.[56] The principle of an active site "memory" was recognized early on,[51] is frequently proven[54,57] and also leveraged e.g., in lipase catalysis.[58] We believe that exploiting this knowledge more often in biocatalysis will unveil powerful enzymes in convergent anionic-, radical-, or cationic rearrangement catalysis, thus making preceding separation techniques obsolete.

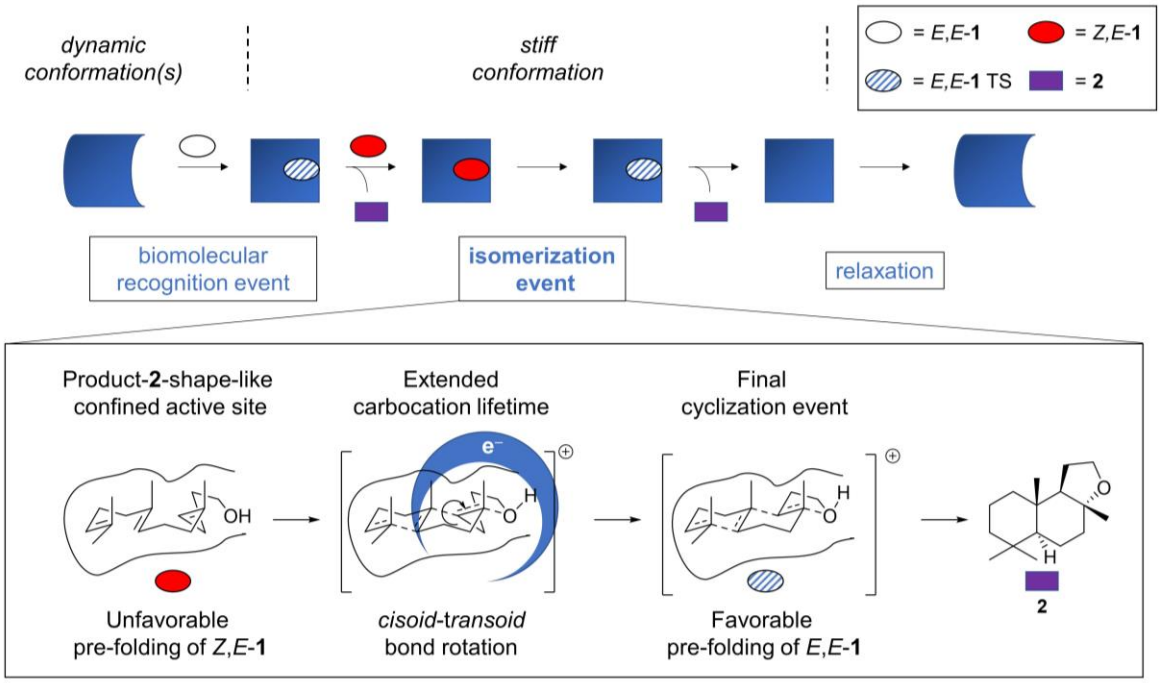

Figure 3: Proposed mechanism for the stereoconvergent cationic cyclization of mix-**1**. Blue shapes represent SHC conformations. After a biomolecular recognition event, the SHC changes its conformation from dynamic to stiff to prepare for catalysis. In this conformation, the restricted active site favors *E,E*-**1** like pre-folding, which facilitates a *cisoid-transoid* bond rotation in synergy with electron density granting ligands (blue circle). Please see Figure S9 for more information on the mechanism.

Engineering the SHC by dual site-allocated mutagenesis for high-performance stereoselective cationic cyclization of *E*,*E*-1.

Having ascertained the exclusive cyclization selective towards **2**, we faced the second issue in SHC catalysis, which is to overcome the generally low catalytic performance. To achieve this overarching aim we further improved the catalytic performance by enzyme engineering while ensuring the exclusive selectivity towards **2** entailing the inherent *in situ* product crystallization (ISPC).[59] We selected the best performing *Aac* W169G, i.e. P1, in combination with *E*,*E*-**1** and began the engineering by one more round of site-saturation mutagenesis in the active site (**Figure 4A**). The final enzyme variants were compared *in vivo* using 100 mM substrate and 10 mg_{CDW}/mL cells to face process conditions (for screening conditions see Figure S11 and 12). To emphasize the engineering, the *Aac* WT and the actual *Aac* benchmark B[36] are also depicted in **Figure 4B**. Screening of 540 generated variants resulted in double-variant W169G/G600M, i.e. P2, which showed 2.7-fold increased turnover frequency (TOF) of 64.6 h^{-1} while retaining >99% **2** selectivity. Further mutations in the active site disrupted the high selectivity of the enzyme, which encouraged us to seek for alternative mutation hot spots, allocated distal from the active site. Consequently, a CAVER analysis of the *Aac* crystal structure was performed and revealed several potential tunnels (Figure S13), of which we focused on the suggested enzyme's entrance tunnel (**Figure 4A**, blue surface).[1] Noteworthy, two (M132R/I432T) out of three positions (M132R/A224V/I432T) of B were located in the designated bottleneck area, with the third position described by the authors themselves as not beneficial.[36] These results gave reason to perform site-saturation mutagenesis within this bottleneck area, which unexpectedly resulted in only slight to no increases in TOF (Figure S14). However, addition of both published distal mutations (M132R/I432T) resulted in the final variant P3 with a 1.3-fold increase in TOF to 87.3 h^{-1} and no loss of selectivity. Stereoconvergence for P3 using mix-**1** was determined with 85% (Figure S15).

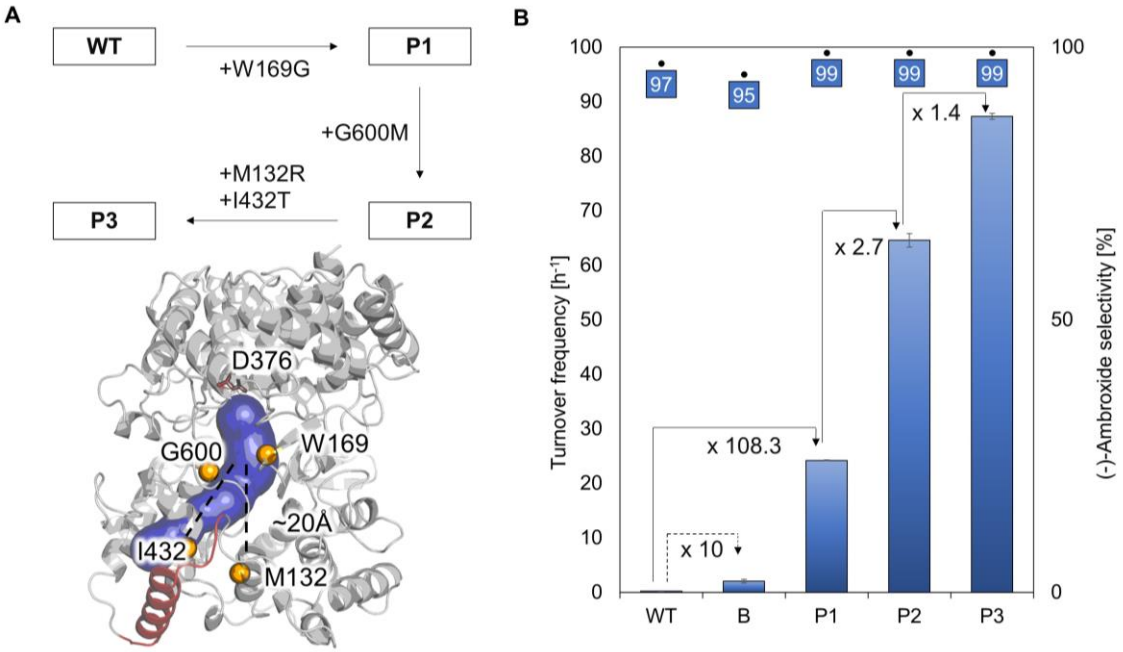

Figure 4: Engineering *Aac* towards highly efficient (–)-ambroxide **2** production under process conditions.[36] **(A)** Structure-guided engineering pathway and crystal structure of *Aac*WT (PDB: 1UMP) with most putative entrance tunnel in blue and membrane binding α-helix in red. Mutated amino acid locations shown as yellow spheres and protonating aspartate as red sticks. Distance of entrance tunnel mutations to functional group of **2** in dashed lines. **(B)** Overall engineering of the *Aac*. Variants are plotted against their turnover frequency (left y-axis) and their (–)-ambroxide **2** selectivity (right y-axis). Reaction conditions: 1 mL *dd*H2O + 0.2% SDS, 10 mg_{CDW} *E. coli* whole-cells harboring the corresponding *Aac* variant (40-50 µM), 100 mM (≈ 50 g/L) *E*,*E*-**1**, 19 h, 30 °C, 750 rpm. Error bars represent the s. d. of technical triplicates. For screening conditions please see Figure S11 and S12.

Summing up, our enzyme engineering efforts improved the overall catalytic performance of the native enzyme by a factor of 397, while ensuring absolute stereocontrol over the cyclization of *E*,*E*-**1**. The catalysis at process conditions clearly benefits from the exclusive **2** selectivity of the enzyme as cytotoxic membrane-disturbing liquid side-products are avoided.[60] The overall catalytic performance was improved by a dual-site allocated mutagenesis approach, which was presented in a similar way by the Reetz group in their engineering of a monoamine oxidase.[61] Such dual allocated approaches extend the strategy of active-site mutagenesis usually conducted in terpene cyclase studies[10,62–64] and are also a useful advancement in the portfolio of rational enzyme engineering strategies.

Computational elucidation of *Aac* P variants' conformational dynamics

In order to rationalize the effects of the introduced active site and distal mutations on the enzyme structure and the accompanied improvement in their catalytic efficiency, a deep computational exploration was performed by means of Molecular Dynamics (MD) simulations (see SI). We reconstructed the conformational landscapes of WT and P variants (see Figure 4), by analyzing the gathered MD data using *Principal Component Analysis* (PCA). The analysis was based on distances between active site residues (6 Å from its center of mass, see SI) to reveal the key active site conformational differences that explain the improved catalytic power of P variants[65].

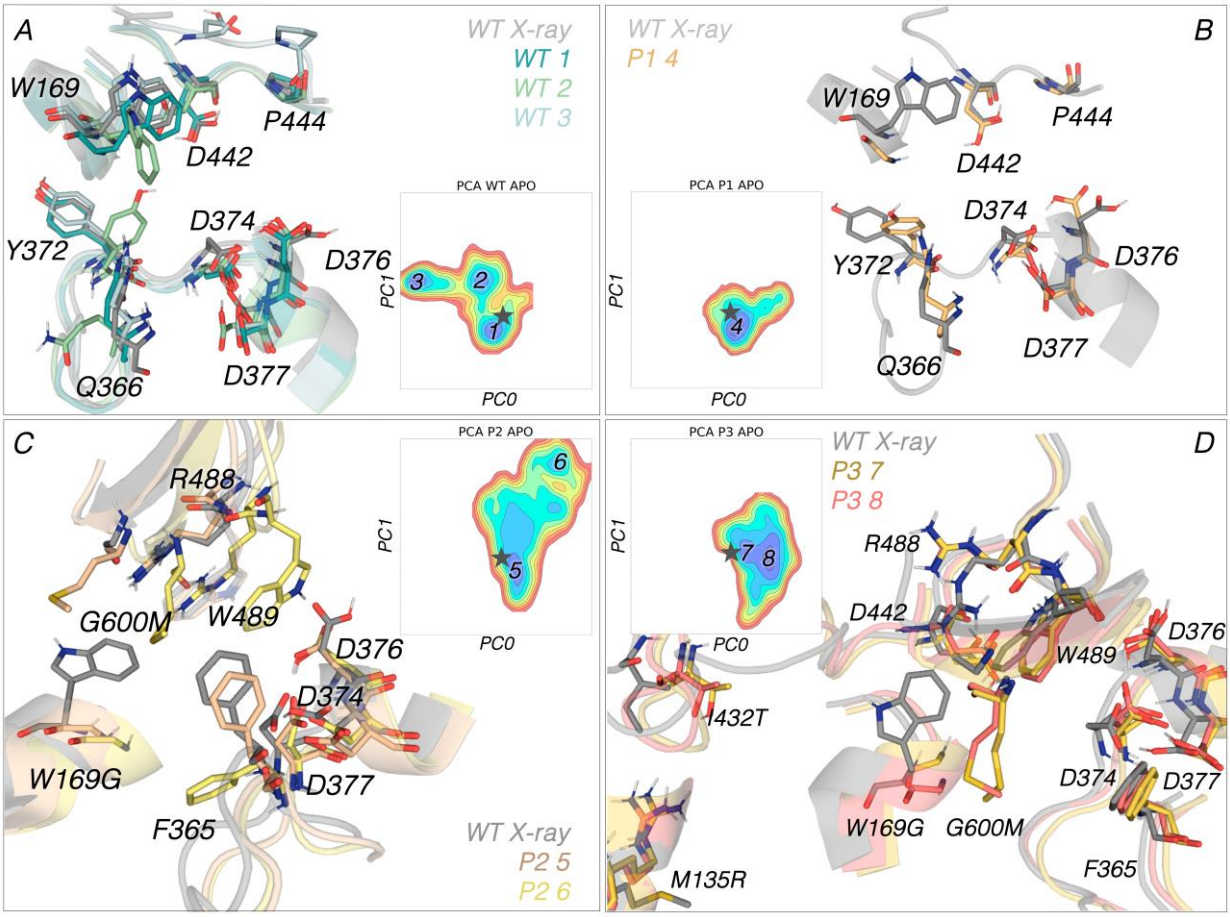

Figure 5: Conformational landscapes of **A)** AaSHC WT, **B)** P1, **C)** P2, and **D)** P3 variants showing the most populated conformations in blue and less populated conformations in red. The grey star in each conformational landscape indicates the position of the crystal structure. Overlay of the different identified active site conformations with respect to the crystal structure (PDB code: 1ump in grey). The most important active site residues are labeled, and different colors are used to represent the different representative conformations extracted from each minimum.

For WT, three main conformations of the active site residues were observed (**Figure 5A**): *conformation 1* displays an X-ray like orientation of the active site residues; *conf. 2* that involves a reshaping of the active site, experienced due to a flip of residues W169, Q366, D442, and Y372; and *conf. 3* that is similar to *1* but presents a different disposition of the loop containing P444. Additionally, a side-chain rotation of F365 that may hamper the accessibility to the catalytic aspartic triad is observed in *conf. 3*.

In case of P1, a single X-ray like active site conformation is explored in the accumulated MD simulation time (**Figure 5B**, conf. 4). The main conformational difference with respect to WT is the rotation of side chain Y372 that interacts with the backbone of residue G169. As illustrated in **Figure 5C**, P2 adopts two main conformations: The X-ray like *conf. 5*, and *conf. 6*, in which a drastic reorganization of the active site is observed. While the W169G mutation alone simply expanded the active site pocket, its combination with mutation G600M results in a dramatic effect on its size and shape. In particular, both mutations act synergistically and introduce a new interaction between R488 and the backbone of mutation G600M. As a consequence, the position of W489 is altered allowing better interaction with the catalytic D376. Finally, the introduced steric bulk at position 600 induces a side-chain rotation of F365. Notwithstanding, and considering the orientation of the latter, this conformation could be impeding the proper access of **2** through the substrate tunnel. As observed for all variants, P3 adopts *conf. 7* that resembles the X-ray like conformation of the active site, and *conf. 8*, which is similar to *conf. 7* (**Figure 5D**). Therefore, the increasing effect of the catalytic efficiency by the distal mutations M132R and I432T may be attributed to the substrate flow and tunnel dynamics that could facilitate the binding process.

Improved substrate tunnel populations lead to more efficient catalysis

To unravel this hypothesis, tunnel analyses were performed on each displayed conformation of WT, P1, P2, and P3 variants, thus having a complete reconstruction of tunnel dynamics along all conformational landscapes. As shown in **Table 1**, the average bottleneck radius (avgBR) is similar in all conformations and systems, which lies between 0.93 and 1.15 Å.

However, drastic differences in the populations of the substrate binding tunnel are obtained, thus indicating that this parameter has been tuned by the mutations introduced along the laboratory-engineering strategy.

Table 1: Tunnels analyses for each conformation of every variant (cf. Figure 5), the average bottleneck radius (avgBR), maximum bottleneck radius (maxBR) in Angstroms, and the percentage of population of the computed substrate binding tunnel are displayed.

Variant	Conformation	avgBR (Å)	maxBR (Å)	Population (%)
WT	1	0.95 ± 0.06	1.19	5
WT	2	0.98 ± 0.07	1.17	3
WT	3	0.97 ± 0.07	1.24	29
P1	4	1.03 ± 0.12	1.45	28
P2	5	1.07 ± 0.13	1.58	29
P2	6	0.93 ± 0.03	1.01	5
P3	7	1.15 ± 0.26	1.83	38
P3	8	1.05 ± 0.15	1.74	58

By analyzing the substrate binding tunnel on each conformation of the WT enzyme we observed low populations for conf. 1 and 2, whereas conf. 3 displayed a higher population of the tunnel (ca. 29%). However, our estimated conformational landscape (cf. Figure 5) suggests this conformation can only be accessed by a relatively high-energy barrier, which may explain the limited catalytic efficiency (cf. Figure 5). The single mutation introduced in P1 enhances the population of the substrate binding tunnel with respect to WT, as a population of 28% is found for the main *conf. 4*, and presents a slightly higher bottleneck radius. Variant P2 can adopt two main conformations: *conf. 5* presenting a tunnel population of 29% and a bottleneck radius of 1.07 Å, and *conf. 6* presenting only 5% of the analyzed snapshots with the main substrate binding tunnel formed. Our estimated conformational landscapes suggest a rather low stability of *conf. 6* with respect to *5*, and a rather high energy barriers for the conformational transition.

Finally, in the case of P3, we observed high populations of the substrate binding tunnel for both conformations: 38% population in *conf. 7,* whereas 58% in *conf. 8*, displaying an average bottleneck radius of ca. 1.1 Å in both conformations. This increase in the tunnel population for the two main conformations adopted by P3 might be one of the main reasons behind the improved activity of P3 with respect to the other engineered P variants.

Mechanistic evidence for improved activity on P variants revealed by *substrate-bound* MD simulations.

In our final investigation we were interested in the ability of the most engineered enzymes to pre-fold **2** in their active sites as well as the resulting conformational changes upon substrate binding. For this purpose, we performed molecular docking of the substrate **2** into the most populated conformations observed in the APO enzymes, followed by MD refinement and conformational landscape reconstruction by analyzing the catalytic distance and angle (Figure S18B). Productive binding was defined by protonating hydrogen (D376) to nucleophile carbon distance D_{prot} below 4.5 Å and an angle Θ_{prot} between 40-60° (**Figure 7A**).[9]

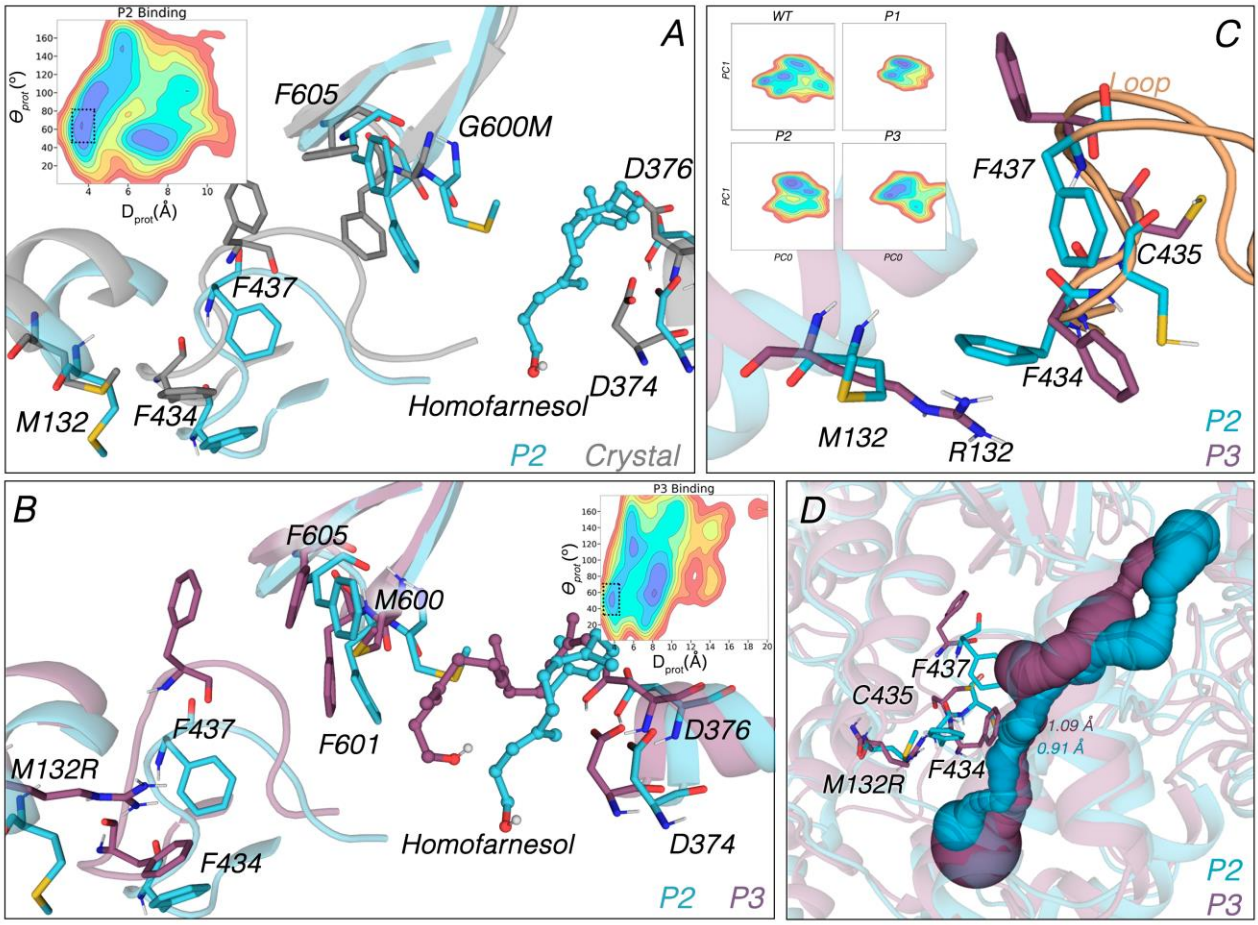

Figure 6: Substrate binding conformational landscape for **A)** P2 and **B)** P3 variants based on the computed catalytic D_{prot} (in Å) and Θ_{prot} (in degrees). Most populated conformations are shown in blue, whereas least populated ones in red. An overlay of representative MD snapshots from the selected regions (marked with dashed black squares) of the binding conformational landscape representing the binding of **2** in the active site for P2 (green) and P3 variants. **C)** Conformational Landscape of the loop containing F434. Overlay of P2 (blue) and P3 (purple) conformations (for a better representation WT and P1 were not included, see Figure S10). Most populated conformations are shown in the conformational landscape in blue, whereas less populated conformations are shown in red. **D)** Overlay of the substrate tunnel in the different conformations of the loop in P2 (blue) and P3 (purple), bottleneck radius are displayed in Angstroms.

When analyzing P2, we again observe the synergy of the two introduced mutations W169G and G600M. The extra room generated by mutation W169G leaves enough space for the G600M side-chain, which is pointing to the center of the active site. This side-chain reorganization is responsible for the better chaperoning of **1**, shortening D_{prot} and improving Θ_{prot}. (**Figure 7B**). Intriguingly, an even more suitable pre-folding of **1** can be observed in P3, which includes the tunnel mutations M132R and I432T ca. 20 Å away. Despite their distance, these mutations drastically affect the size and shape of the catalytic pocket by means of a

network of interactions that lead to side-chain reorganizations. More specifically, M132R (in combination with all other mutations) seem to be responsible for triggering such reorganization (**Figure 5B**). The new arginine side chain introduced (M132R) is able to interact with the backbone of residue F434. This new interaction between R132 and F434 leads to a flip in the loop containing F437, which generates extra space that is occupied by the side-chain of F605. This results in a higher flexibility of M600 that enables **1** to adopt more pre-folded conformations, with improved D_{prot} and Θ_{prot}.

The new network of interactions in P3 may be stabilizing wider substrate tunnels in P3 variant, which could be translated in higher displayed activities over P2. To unravel this hypothesis, PCA analyses were conducted on the loop containing residue F437, aiming to determine which conformations are mainly adopted by each variant (**Figure 5C** and Figure S19). As we observed in **1**-bound MD simulations, mutation M132R in P3 variant is stabilizing the X-ray like orientation of the loop. This new mutation produces a flip in residue F434, which alters the backbone dihedral of residue C435. Furthermore, the latter determines the orientation of the side chain of residue F437. This network of coupled conformational changes produces a wider substrate tunnel that is reflected in the previously analyzed tunnels (**Figure 5D**). Interestingly, the conformations of the F434-containing loop that resemble to the X-ray structure resulted in a pre-folded binding of **1** in case of P3, whereas in the case of P2 there is a flip on this F434-loop that induces the stretching and unbinding of **1** (cf. Figure 5B). Indeed, F437 and C435 residues were previously identified as key gating residues in a previous study, which is also supported by our MD simulations.[10]

Taking our computational results together, we demonstrated that the active site mutations are mainly responsible for the reorganization of the active site and improved chaperoning of **1** especially in P2 and P3 variants, whereas the tunnel mutations are mainly responsible for an improved substrate flux stabilizing X-ray like conformations of the loop containing F434. These findings suggest how we achieved the 397-fold improved catalytic by

tailoring the supramolecular and dynamic SHC scaffold for a 'open tunnel' catalyst with improved substrate flux and chaperoning.

Kinetic comparison of the *Aac* variants and the turnover limits of the SHC

With this efficient enzyme in hands, the next step to achieve the overarching aim to cross the SHC's turnover boundaries was to investigate the enzyme's performance employing high substrate/cell or catalyst ratios. After some initial experiments that demonstrated a cell concentration-dependent activity (Figure S16), the four *Aac* variants WT, B, P2 and P3 were kinetically analyzed *in vivo* and *in vitro* (**Figure 7A+B**). These variants were chosen as they comprise the four stages of engineering: Native enzyme, engineered entrance tunnel, engineered active site and engineered active site + entrance tunnel. Starting with the *in vitro* characterization, it is worth to mention that membrane-bound enzymes require detergents as an artificial membrane for isolation and solubilization, which may influence their catalytic activity.[42,66,67] The evaluation showed that the entrance tunnel mutations of the benchmark SHC B doubled the k_{cat}, while only slightly affecting K_M and therefore substrate affinity (**Table 4,** B, *in vitro*). In P2, the alterations highly increased the substrate affinity and thus lowered the K_M 5-fold, which entailed a ~12-fold increase in k_{cat} (**Table 4,** P2, *in vitro*). Finally, the additional entrance tunnel mutations in P3 resulted in almost doubled k_{cat}, while K_M remained almost unchanged. In total, the structure-guided engineering of the WT in the active site and entrance tunnel led to a catalytic efficiency k_{cat}/K_M of 372.5 mM*min^{-1} (**Table 4,** P3, *in vitro*), which is an improvement of more than 250-fold. Remarkably, our experimental findings directly align with our computational data that ascribed increased substrate flow mainly to the distal mutations

Table 4: Parameters of initial rate kinetics for *Aac* WT and variants B, P2 and P3 *in vitro* and *in vivo*. The *in vitro* kinetics were approximated by Michaelis-Menten plots. The *in vivo* kinetics were approximated by substrate-excess inhibition plots.

	in vitro			***in vivo***		
	K_M [mM]	k_{cat} [min^{-1}]	k_{cat}/K_M [mM*min^{-1}]	$K_{M,app}$ [mM]	$k_{cat,app}$ [min^{-1}]	$k_{cat,app}/K_{M,app}$ [mM*min^{-1}]
WT	0.94	1.38	1.47	0.16	0.52	3.14
B	1.06	2.81	2.65	0.17	0.60	3.44
P2	0.19	35.65	185.95	0.22	26.32	117.01
P3	0.16	61.62	372.48	0.21	28.70	135.12

Noteworthy, all initial rate kinetics *in vitro* could be approximated by Michaelis-Menten plots (**Figure 7A**). In contrast, the *in vivo* kinetics had to be approximated by substrate-excess-inhibition plots with the inhibition constant $K_i = K_{M,app}$ occurring at ~0.21 mM for all characterized variants (**Figure 7B+C**). Nevertheless, a 45-fold increase in catalytic efficiency of P3 ($k_{cat,app}/K_{M,app}$ ~ 135 mM*min^{-1}) compared to the WT was determined (**Table 4,** P3, *in vivo*). Interestingly, the strong inhibition was lowered by reducing the orbital shaking from 800 to 600 to 300 rpm to the expense of a 9-fold lower catalytic efficiency $k_{cat,app}/K_{M,app}$ of ~15 (Figure S17).

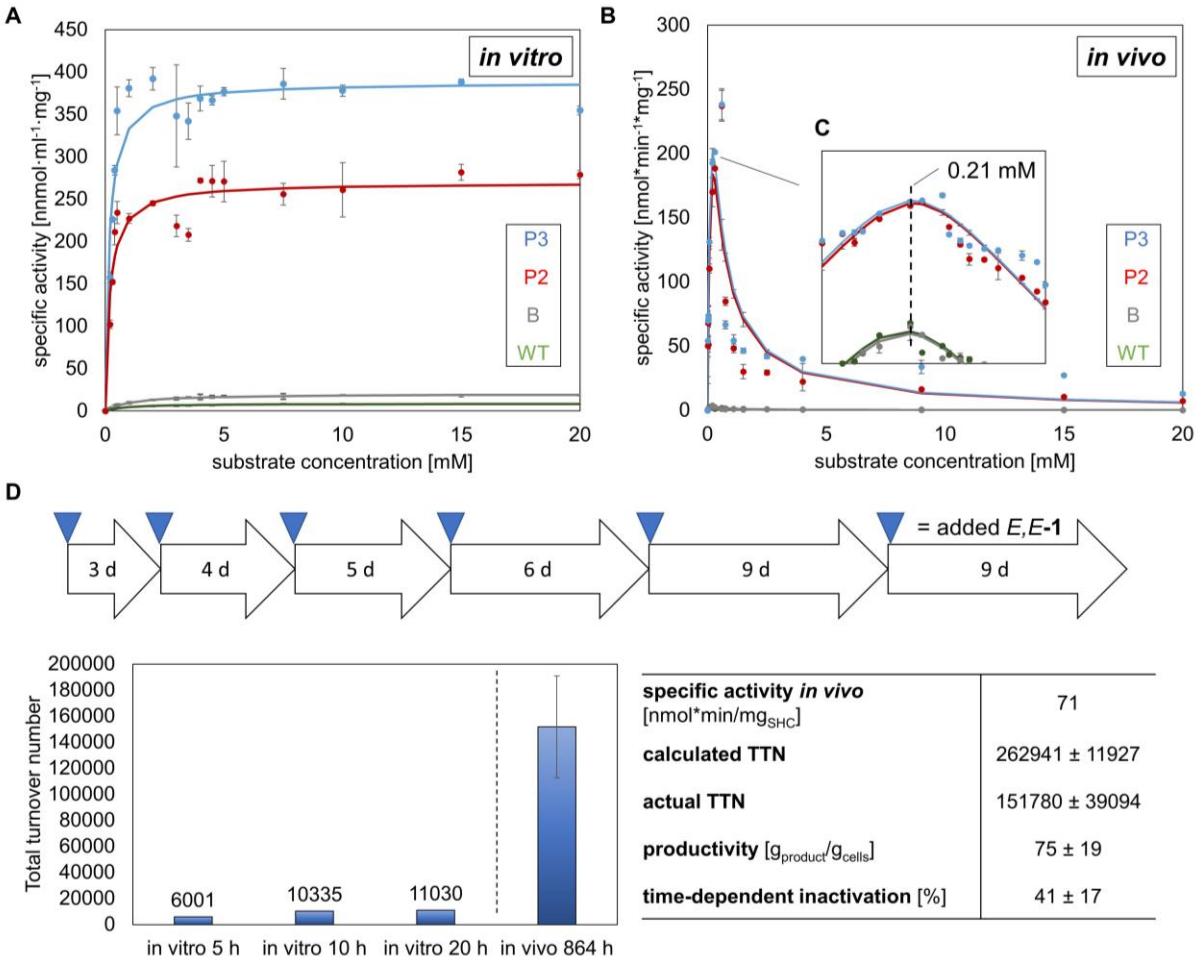

Figure 7: Crossing the turnover boundaries of the SHC. (**A**) Michaelis-Menten plots for the *Aac* WT, B, P2, and P3 catalyzed cyclization of *E*,*E*-**1** *in vitro.* (**B**) Substrate-excess inhibition plots for the *Aac* WT, B, P2, and P3 catalyzed cyclization of *E*,*E*-**1** *in vivo*. (**C**) Double-logarithmic plot of substrate concentration vs. specific activity. Error bars represent the s. d. between technical triplicates. (**D**) Feeding strategy for max. total turnover (TTN) of *E*,*E*-**1** with an engineered P3 driven by continuous ISPC. Arrows only apply for long term *in vivo* approach. Calculated TTN was

determined assuming the specific activity of 71 nmol*min/mg_{SHC}, which was taken from Figure S17. Please see supporting information for detailed reaction conditions and control.

With this knowledge about the enyzme kinetics, the stage was set to cross the turnover boundaries of the SHC. To that end, we envisaged a feeding strategy exploiting the enzyme's stereoconvergence and the continuous ISPC of **2**. An enzyme solution (0.015 mg/ml SHC, 0.2% CHAPS, 20 mM citric acid, pH = 6.0) and whole-cell suspension (0.1 g_{CDW} /L in *dd*H_2O) were prepared, supplemented with 200 µL (7 mM) pure *E*,*E*-**1** and shaken at 300 rpm and depletion of the substrate layer was observed. The substrate concentration was selected as it depicts the concentration before the inhibited and non-inhibited *in vivo* plots cross-over (cf. Figure S17). During the *in vitro* approaches almost no depletion occurred, and the reactions stopped after ~10 h and ~3.5% product formation, which equals a total turnover number of ~11000. Intriguingly, the SHC in the whole cells was active for 34-38 days using the feeding strategy (**Figure 7D**). Thus, a total turnover number (TTN) of an average of ~150000 was achieved. Compared to the calculated TTN of 262941, the enzyme lost ~41% of its activity, indicating a time-dependent inactivation of the catalyst. Overall, ~0.75 g of the desired product (–)-ambroxide **2** could be produced employing only 10 mg of *E. coli* whole cells (**Figure 7D**). To further demonstrate industrial feasibility, 100 g/L **2** were produced within 96 h using 50 g_{CDW}/L cells in pure *dd*H_2O (Figure S18).

Overall, the kinetic data disclosed meaningful differences of the enzyme's catalytic behavior *in vivo* and *in vitro*. In their natural membrane environment, all SHC variants are strongly inhibited after the peak performance concentration of 0.21 mM which suggests a regulative function of the lipid environment on the enzymatic activity. This inseparable relationship was recently demonstrated in the reconstitution of the *in vitro* activity of the membrane-bound particulate monooxygenase by mimicking the natural lipid environment.[68] Due to their inherent hydrophobicity, terpenes diffuse into the cell membrane presumably causing local perturbations, whereupon the enzyme reacts downregulating its activity. This regulatory function by sensing membrane integrity would be a simple tool for nature to control activity of membrane-bound enzymes as already hypothesized in 1975.[69] To omit the

downregulation, the local perturbations have to be 'widespread' by offering the terpenes more membrane area which can be achieved by the invagination of the cellular membrane[70] or simply by increasing the cell concentration.[36] The feeding strategy combined with the exclusive selectivity and the in situ product crystallization of the sole **2** kept the enzyme stable for several weeks, performing over 10^6 turnovers, which supersedes all so far reported TTNs of SHCs[21,36,71] and unveils the true potential of these enzymes. Furthermore, biocatalysts exhibiting turnover numbers in the 10^6 range are well positioned among the upper ranks of industrially applied enzymes.[37,72] However, an apparent drawback is the long time period of the presented process, which could be overcome by increasing the mass transfer across the biomembrane using membrane transporter enzymes[73] or spheroplast preparation.[74] Furthermore, the herein presented *in vitro* approach could certainly be fine-tuned by changing deteregent, detergent concentration or buffer, however, was beyond the scope of this study.

Conclusion & outlook

The study of terpene cyclases substantially contributed to historical innovations in enzymology synthetic and mechanistic chemistry.[4,39,75,76] In this study we have demonstrated how to tailor and leverage the structural and chemical biology of SHCs to perform catalysis beyond their currently known capabilities. Stereoconvergent cyclizations are genetically encoded in these enzymes, are aided by conformational enzyme dynamics and can be fine-tuned by creating a locally electron enriched confinement around the substrate. Total turnover boundaries can be crossed by widening the enzyme's tunnel, increasing substrate flow, and considering its membrane-bound nature. Going forward, the active site memory effect will be further examined and the exact amino acid contributions enabling the stereoconvergent cyclization will be analyzed using detailed QM/MM studies. This knowledge could then be transferred to synthetic catalysts or *de novo* enzyme design tools, such as Rosetta.[77] The exact mechanism of the substrate-induced downregulation will be elucidated in detail by studying the membrane's properties during catalysis, e.g. by fluorescence imaging.[78] Assuming such an indirect downregulation of monotopically membrane-bound enzymes, opens up alternative views on

diseases related to similar enzymes such as the visual impairment, Alzheimer's or Parkinson's disease.[79–83] To say it in the words of Engasser and Horvath: "*It is unlikely that nature would not use such a simple tool to control and trigger physiological processes".*[30]

Acknowledgements

The authors thank Lea Rapp and Peter Heinemann for fruitful discussions. We thank Benjamin Aberle for preparative HPLC isolation of pure *Z,E*-homofarnesol. We gratefully acknowledge the Deutsche Forschungsgemeinschaft (DFG HA 1251/6-1) for research funding. A.S., B.H. and S.O. planned the overall project. A.S. and T.L. conducted experimental work. C.C. conducted computational work. A.S., C.C., B.H. and S.O. drafted the manuscript. All authors agreed on the final manuscript.

Conflict of interest

There are conflicts of interest to declare.

References

[1] K. U. Wendt, K. Poralla, G. E. Schulz, *Science* **1997**, *277*, 1811–1815.

[2] C. M. Starks, K. Back, J. Chappell, J. P. Noel, *Science* **1997**, *277*, 1815–1820.

[3] C. A. Lesburg, G. Zhai, D. E. Cane, D. W. Christianson, *Science* **1997**, *277*, 1820–1824.

[4] Y. J. Hong, D. J. Tantillo, *Nat. Chem.* **2009**, *1*, 384–389.

[5] D. J. Tantillo, *Nat. Prod. Rep.* **2011**, *28*, 1035–1053.

[6] R. Rajamani, J. Gao, *J. Am. Chem. Soc.* **2003**, *125*, 12768–12781.

[7] P. R. Wilderman, R. J. Peters, *J. Am. Chem. Soc.* **2007**, *129*, 15736–15737.

[8] A. Schneider, P. Jegl, B. Hauer, *Angew. Chemie - Int. Ed.* **2021**, *60*, 13251–13256.

[9] S. C. Hammer, P.-O. Syrén, B. Hauer, *ChemistrySelect* **2016**, *1*, 3589–3593.

[10] T. Sato, M. Kouda, T. Hoshino, *Biosci. Biotechnol. Biochem.* **2004**, *68*, 728–738.

[11] M. Seitz, J. Klebensberger, S. Siebenhaller, M. Breuer, G. Siedenburg, D. Jendrossek, B. Hauer, *J. Mol. Catal. B Enzym.* **2012**, *84*, 72–77.

[12] M. Seitz, P. O. Syrén, L. Steiner, J. Klebensberger, B. M. Nestl, B. Hauer, *ChemBioChem* **2013**, *14*, 436–439.

[13] S. A. Bastian, S. C. Hammer, N. Kreß, B. M. Nestl, B. Hauer, *ChemCatChem* **2017**, *9*, 4364–4368.

[14] I. Abe, H. Tanaka, H. Noguchi, *J. Am. Chem. Soc.* **2002**, *124*, 14514–14515.

[15] H. Tanaka, H. Noma, H. Noguchi, I. Abe, *Tetrahedron Lett.* **2006**, *47*, 3085–3089.

[16] T. Hoshino, Y. Kumai, I. Kudo, S. I. Nakano, S. Ohashi, *Org. Biomol. Chem.* **2004**, *2*, 2650–2657.

[17] S. C. Hammer, A. Marjanovic, J. M. Dominicus, B. M. Nestl, B. Hauer, *Nat. Chem. Biol.* **2015**, *11*, 121–126.

[18] S. Henche, B. M. Nestl, B. Hauer, *ChemCatChem* **2021**, *13*, 3405–3409.

[19] P. O. Syren, S. Henche, A. Eichler, B. M. Nestl, B. Hauer, *Curr. Opin. Struct. Biol.* **2016**, *41*, 73–82.

[20] M. Jia, R. J. Peters, *Org. Biomol. Chem.* **2017**, *15*, 3158–3160.

[21] M. Eichenberger, S. Hüppi, D. Patsch, N. Aeberli, R. Berweger, S. Dossenbach, E. Eichhorn, F. Flachsmann, L. Hortencio, F. Voirol, S. Vollenweider, U. T. Bornscheuer, R. Buller, *Angew. Chemie - Int. Ed.* **2021**, *60*, 26080–26086.

[22] H. F. Kasai, M. Tsubuki, Y. Matsumoto, M. Shirao, K. Takahashi, T. Honda, H. Ueda, *Chem. Pharm. Bull* **2004**, *52*, 311–315.

[23] J. C. Coli, B. F. Bowden, *J. Nat. Prod.* **1986**, *49*, 934–936.

[24] D. J. Reinert, G. Balliano, G. E. Schulz, *Chem. Biol.* **2004**, *11*, 121–126.

[25] P. Baer, P. Rabe, K. Fischer, C. A. Citron, T. A. Klapschinski, M. Groll, J. S. Dickschat, *Angew. Chemie - Int. Ed.* **2014**, *53*, 7652–7656.

[26] K. N. Allen, S. Entova, L. C. Ray, B. Imperiali, *Trends Biochem. Sci.* **2019**, *44*, 7–20.

[27] D. Darland, T. D. Brock, *Bacillus Acidocaldarius Sp.Nov., an Acidophilic Thermophilic Spore-Forming Bacterium*, **1971**.

[28] K. Poralla, E. Kannenberg, A. Blume, *FEBS Lett.* **1980**, *113*, 107–110.

[29] B. J. Belin, N. Busset, E. Giraud, A. Molinaro, A. Silipo, Di. K. Newman, *Nat. Rev. Microbiol.* **2018**, *1*, 304–315.

[30] J.-M. Engasser, C. Horvath, *Biochemistry* **1974**, *13*, 26.

[31] K. Balali-Mood, P. J. Bond, M. S. P. Sansom, *Biochemistry* **2009**, *48*, 2135–2145.

[32] H. S. Camargos, R. A. Moreira, S. A. Mendanha, K. S. Fernandes, M. L. Dorta, A. Alonso, *PLoS One* **2014**, *9*, DOI 10.1371/journal.pone.0104429.

[33] F. Harb, L. Prunetti, M. T. Giudici-Orticoni, M. Guiral, B. Tinland, *Eur. Phys. J. E* **2015**, *38*, 1–11.

[34] A. H. Pande, S. Qin, S. A. Tatulian, *Biophys. J.* **2005**, *88*, 4084–4094.

[35] A. Laganowsky, E. Reading, T. M. Allison, M. B. Ulmschneider, M. T. Degiacomi, A. J. Baldwin, C. V Robinson, *Nature* **2014**, *510*, DOI 10.1038/nature13419.

[36] E. Eichhorn, E. Locher, S. Guillemer, D. Wahler, L. Fourage, B. Schilling, *Adv. Synth. Catal.* **2018**, *350*, 2339–2351.

[37] S. Wu, R. Snajdrova, J. C. Moore, K. Baldenius, U. T. Bornscheuer, *Angew. Chemie - Int. Ed.* **2021**, *60*, 88–119.

[38] C. Klaus, S. C. Hammer, *Trends Chem.* **2022**, 1–4.

[39] R. Properzi, P. S. J. Kaib, M. Leutzsch, G. Pupo, R. Mitra, C. K. De, L. Song, P. R. Schreiner, B. List, *Nat. Chem.* **2020**, *12*, 1174–1179.

[40] Q. Zhang, K. Tiefenbacher, *Nat. Chem.* **2015**, *7*, 197–202.

[41] Q. Zhang, L. Catti, J. Pleiss, K. Tiefenbacher, *J. Am. Chem. Soc.* **2017**, *139*, 11482–11492.

[42] S. Neumann, H. Simon, *Biol. Chem. Hoppe. Seyler.* **1986**, *367*, 723–730.

[43] M. Breuer, A. Hörster, B. Hauer, *Biocatalytic Production of Ambroxan; U.S. Patent No. 8,759,043. 24 Jun. 2014.*, **2014**.

[44] S. J. Rowland, P. A. Sutton, T. D. J. Knowles, *Nat. Prod. Res.* **2019**, *33*, 3134–3142.

[45] K. Ishihara, H. Ishibashi, H. Yamamoto, *J. Am. Chem. Soc.* **2002**, *124*, 3647–3655.

[46] S. Merget, L. Catti, G. Piccini, K. Tiefenbacher, *J. Am. Chem. Soc.* **2020**, *142*, 4400–4410.

[47] L. Smentek, B. A. Hess, *J. Am. Chem. Soc.* **2010**, *132*, 17111–17117.

[48] R. P. Pemberton, D. J. Tantillo, *Chem. Sci.* **2014**, *5*, 3301–3308.

[49] M. Weitman, D. T. Major, *J. Am. Chem. Soc.* **2010**, *132*, 6349–6360.

[50] J. RICARD, J. -C MEUNIER, J. BUC, *Eur. J. Biochem.* **1974**, *49*, 195–208.

[51] B. R. Rabin, *Biochem. J.* **1967**, *102*, 22C-23C.

[52] J. P. Richard, *J. Am. Chem. Soc.* **2019**, *141*, 3320–3331.

[53] D. D. Boehr, R. Nussinov, P. E. Wright, *Nat. Chem. Biol.* **2009**, *5*, 789–796.

[54] H. P. Lu, *Science* **1998**, *282*, 1877–1882.

[55] P. O. Syrén, S. C. Hammer, B. Claasen, B. Hauer, *Angew. Chemie - Int. Ed.* **2014**, *53*, 4845–4849.

[56] D. A. Whittington, M. L. Wise, M. Urbansky, R. M. Coates, R. B. Croteau, D. W. Christianson, *Proc. Natl. Acad. Sci. U. S. A.* **2002**, *99*, 15375–15380.

[57] R. Pan, X. J. Zhang, Z. J. Zhang, Y. Zhou, W. X. Tian, R. Q. He, *J. Biol. Chem.* **2010**, *285*, 22950–22956.

[58] D. Lee, Y. K. Choi, M. J. Kim, *Org. Lett.* **2000**, *2*, 2553–2555.

[59] D. Hülsewede, L. E. Meyer, J. von Langermann, *Chem. - A Eur. J.* **2019**, *25*, 4871–4884.

[60] H. H. Agus, in *Toxicology*, Academic Press, **2021**, pp. 33–42.

[61] G. Li, P. Yao, R. Gong, J. Li, P. Liu, R. Lonsdale, Q. Wu, J. Lin, D. Zhu, M. T. Reetz, *Chem. Sci.* **2017**, *8*, 4093–4099.

[62] T. Hoshino, K. Shimizu, T. Sato, *Angew. Chemie - Int. Ed.* **2004**, *43*, 6700–6703.

[63] M. Xu, P. R. Wilderman, R. J. Peters, *Proc. Natl. Acad. Sci. U. S. A.* **2007**, *104*, 7387–7401.

[64] K. C. Potter, J. Zi, Y. J. Hong, S. Schulte, B. Malchow, D. J. Tantillo, R. J. Peters, *Angew. Chemie - Int. Ed.* **2016**, *55*, 634–638.

[65] M. A. Maria-Solano, E. Serrano-Hervás, A. Romero-Rivera, J. Iglesias-Fernández, S. Osuna, *Chem. Commun.* **2018**, *54*, 6622–6634.

[66] P. M. Rodi, M. D. Bocco Gianello, M. C. Corregido, A. M. Gennaro, *Biochim. Biophys. Acta - Biomembr.* **2014**, *1838*, 859–866.

[67] V. Kotov, K. Bartels, K. Veith, I. Josts, U. K. T. Subhramanyam, C. Günther, J. Labahn, T. C. Marlovits, I. Moraes, H. Tidow, C. Löw, M. M. Garcia-Alai, *Sci. Rep.* **2019**, *9*, DOI 10.1038/s41598-019-46686-8.

[68] C. W. Koo, F. J. Tucci, Y. He, A. C. Rosenzweig, *Science* **2022**, *375*, 1287–1291.

[69] R. N. Farías, B. Bloj, R. D. Morero, F. Siñeriz, R. E. Trucco, *Biochim. Biophys. Acta - Rev. Biomembr.* **1975**, *415*, 231–251.

[70] Y. Meng, X. Shao, Y. Wang, Y. Li, X. Zheng, G. Wei, S. W. Kim, C. Wang, *Biotechnol. Bioeng.* **2020**, *1*, 1–9.

[71] S. C. Hammer, A. Marjanovic, J. M. Dominicus, B. M. Nestl, B. Hauer, *Nat. Chem. Biol.* **2015**, *11*, 121–126.

[72] B. Hauer, *ACS Catal.* **2020**, *10*, 8418–8427.

[73] M. K. Julsing, M. Schrewe, S. Cornelissen, I. Hermann, A. Schmid, B. Bühler, *Appl. Environ. Microbiol.* **2012**, *78*, 5724–5733.

[74] A. I. Benítez-Mateos, A. Schneider, E. Hegarty, B. Hauer, F. Paradisi, *ChemRxiv* **2022**, DOI 10.26434/CHEMRXIV-2022-W08D0.

[75] K. Ishihara, S. Nakamura, H. Yamamoto, *J. Am. Chem. Soc.* **1999**, *121*, 4906–4907.

[76] I. Čorić, B. List, *Nature* **2012**, *483*, 315–319.

[77] F. Richter, A. Leaver-Fay, S. D. Khare, S. Bjelic, D. Baker, *PLoS One* **2011**, *6*, e19230.

[78] P. Weber, M. Wagner, H. Schneckenburger, *J. Biomed. Opt.* **2010**, *15*, 046017.

[79] P. D. Kiser, M. Golczak, D. T. Lodowski, M. R. Chance, K. Palczewski, *Proc. Natl. Acad. Sci. U. S. A.* **2009**, *106*, 17325–17330.

[80] M. Golczak, P. D. Kiser, D. T. Lodowski, A. Maeda, K. Palczewski, *J. Biol. Chem.* **2010**, *285*, 9667–9682.

[81] P. H. Nguyen, A. Ramamoorthy, B. R. Sahoo, J. Zheng, P. Faller, J. E. Straub, L. Dominguez, J. E. Shea, N. V. Dokholyan, A. de Simone, B. Ma, R. Nussinov, S. Najafi, S. T. Ngo, A. Loquet, M. Chiricotto, P. Ganguly, J. McCarty, M. S. Li, C. Hall, Y. Wang, Y.

Miller, S. Melchionna, B. Habenstein, S. Timr, J. Chen, B. Hnath, B. Strodel, R. Kayed, S. Lesné, G. Wei, F. Sterpone, A. J. Doig, P. Derreumaux, *Chem. Rev.* **2021**, *121*, 2545–2647.

[82] M. Ashtari, E. S. Nikonova, K. A. Marshall, G. J. Young, P. Aravand, W. Pan, G. shuang Ying, A. E. Willett, M. Mahmoudian, A. M. Maguire, J. Bennett, *Ophthalmology* **2017**, *124*, 873–883.

[83] E. Winkler, F. Kamp, J. Scheuring, A. Ebke, A. Fukumori, H. Steiner, *J. Biol. Chem.* **2012**, *287*, 21326–21334.